文章编号：1001-9014(XXXX)XX-0001-12

DOI：10. 11972/j. issn. 1001-9014. JIMW. 2026171

Broadband and uniform-response MCNO bolometer based on MXene/CNTs/SiC composites from visible to terahertz

Chen Bing[1,2], Gao Yan-Qing[2,3], Lei Si-Yuan[2,3], Chi Ling-Ze[1,2], Leng Cheng-Yu[6], Yang Bo[5], Jiang Lin[3], Yao Niang-Juan[3], Liu Yi[2,4], Zhou Wei[2,3*], Yin Xiong-Fei[1,2*], Huang Zhi-Ming[1,2,3*], Chu Jun-Hao[3]

(1. Hangzhou Institute for Advanced Study, UCAS, Hangzhou 310024, China;
2. University of Chinese Academy of Sciences, Beijing 100049, China;
3. State Key Laboratory of Infrared Physics, Shanghai Institute of Technical Physics, Chinese Academy of Sciences, Shanghai 200083, China;
4. Ningbo Institute of Materials Technology and Engineering, Ningbo 315201, China;
5. School of Physics, Huazhong University of Science and Technology, Wuhan 430074, China;
6. School of Microelectronics, Shanghai University, Shanghai 201804, China)

Abstract: Development of broadband detectors is crucial for applications such as non-destructive imaging, biosensing and next-generation communications. Here, a broadband $Mn_{1.56}Co_{0.96}Ni_{0.48}O_4$ (MCNO) bolometer with an MXene/CNTs/SiC composite absorber is developed, whose uniform response is verified at four representative wavelengths. An ultrathin "black paint (BP)-SiC-BP" sandwich composite coating is designed, where the BP is composed of MXene/CNTs mixture with MXene : CNTs=1 : 2. The MCNO detector with the composite absorber achieves an average responsivity of 35. 9±1. 8 V/W at a modulation frequency of 2 Hz from four independent measurements at 0. 635, 1. 55, 10. 6 and 880 μm, corresponding to a response uniformity of approximately 95%. Its broadband response originates from the cascaded absorption of the MXene/CNTs composite and the optical-path extension induced by the SiC intermediate layer. Consequently, the device exhibits a noise equivalent power (NEP) of 3×10^{-9} W/Hz$^{0.5}$ and a thermal time constant of about 143. 7 ms.

Key words: Broadband photodetector, MCNO bolometer, MXene/CNTs/SiC composites, Vis - THz
PACS:

Introduction

Broadband photodetection is crucial for advanced optoelectronic systems, and its advancement is critical for high-speed communication, non-destructive imaging, biosensing and other key applications[1-6]. High-efficiency broadband absorption constitutes the fundamental prerequisite for achieving high-performance broadband detection. Conventional bolometers suffer from selective absorption and complex fabrication, limiting their performance and applications. Furthermore, the lack of ultrathin materials for strong broadband absorption is a critical bottleneck for broadband detection. The overall performance of a bolometer is largely determined by two key components: the absorber layer, which governs the efficiency of light harvesting, and the thermosensitive layer, which converts the absorbed radiation into an electrical signal.

To achieve broadband optical absorption, various strategies have been explored. Metallic or metasurface-based resonators can realize near-perfect absorption at specific frequencies, yet their intrinsic bandwidth is fundamentally constrained by the resonant electromagnetic modes, making it difficult to cover spectral ranges exceeding a decade in frequency. Moreover, their complex microfabrication processes hinder large-area, cost-effective production[7-10]. Carbon nanotube (CNT) films, owing to their unique one-dimensional conjugated structure, exhibit relatively broad terahertz (THz) absorption bands[11-16]; however, their impedance matching characteristics remain unsatisfactory in the lower-frequency range, leaving considerable room for improvement in absorptivity. More recently, MXenes, an emerging family of two-dimensional transition metal carbides and nitrides, have shown strong THz absorption, which is attributed to their high carrier concentration, short carrier relaxation time, and abundant surface functional groups[17-21]. However, compact MXene films suffer from severe impedance mismatch due to their high electrical

Received date: 2026-XX-XX, 收稿日期：2026-录用日期：2026-
Foundation items: Supported by Shanghai Natural Science Foundation (Grant No. 25ZR1401376), Open Fund of State Key Laboratory of Infrared Physics (Grant No. SITP-NLIST-YB-2024-06) and National Natural Science Foundation of China (Grant 62588101).
* **Corresponding author**: E-mail: zmhuang@mail. sitp. ac. cn

conductivity. To overcome this limitation, we fabricate composite absorption coatings by combining MXene dispersion with carbon nanotubes (CNTs) at an optimized ratio[22] thereby leveraging the advantages of both components to achieve efficient broadband absorption.

On the detection side, the thermosensitive material is equally critical for device performance. $Mn_{1.56}Co_{0.96}Ni_{0.48}O_4$ (MCNO), a transition metal oxide semiconductor, offers excellent thermal stability and a stable negative temperature coefficient of resistance (TCR) over 200 – 350 K, making it an ideal candidate for uncooled infrared and THz detection[23-25]. However, pristine MCNO films exhibit intrinsically weak absorption from visible to THz, severely limiting their detection capability without an efficient light-absorbing layer. Therefore, an ultra-thin "black paint" layer—a composite of MXene and CNTs is coated onto the MCNO sensing element to enhance the effective absorption[26-27].

In this study, an ultra-thin (<0.1 mm) "black paint (BP) – SiC – BP" sandwich-structured composite absorbing coating is designed and fabricated on MCNO thermistor films. The upper and lower BP layers are composed of MXene and CNTs mixed at an optimized ratio of 1∶2, aiming to construct a cascaded conductive network where broadband ohmic and dielectric losses covering the representative wavelengths from visible to THz are synergistically generated by the two-dimensional MXene flakes and one-dimensional CNT bundles. An intermediate SiC particle layer is introduced to exploit its high refractive index, by which multiple scattering of THz waves within the coating is enhanced and the effective optical path length is extended[28]. Experimental results show that this ternary synergistic design overcomes the frequency-band limitations of any single component, enabling broadband and uniform absorption across an ultrabroad spectral range of 150 – 7500 cm^{-1}. The morphology, optical reflectance, and electrical response of the composite coating are systematically characterized. At a modulation frequency of 2 Hz, four independent measurements at 0.635, 1.55, 10.6 and 880 μm give an average responsivity of 35.9±1.8 V/W, corresponding to a response uniformity of approximately 95%. A feasible technical pathway for the design of absorbing layers in next-generation broadband thermal detectors is provided by this work, and key material support for uncooled multi-band integrated detection systems is also offered.

2 Materials and Methods

2.1 Preparation of MCNO Thin Films

Powders of manganese acetate, cobalt acetate and nickel acetate were mixed at a molar ratio of 1.56∶0.96∶0.48, and the $Mn_{1.56}Co_{0.96}Ni_{0.48}O_4$ polycrystalline target was prepared by the cold pressing and sintering method. Subsequently, MCNO thin films were deposited on square sapphire substrate and gold substrates using a radio frequency magnetron sputtering system. During the sputtering process, the base vacuum was set to 1.7×10^{-7} Torr, the sputtering power to 50 W, and the substrate growth temperature was controlled below 450 ℃.

The thickness of the sapphire substrate was 80 μm, the deposition thickness of the thin film was 10 μm, and that on the gold substrate was 1.5 μm, with a sputtering rate of approximately 1.4 nm/min. After the film deposition, a subsequent annealing treatment was carried out at 750 ℃ for 30 minutes in the atmospheric environment.

2.2 Preparation of Composite Coatings with Different Ratios

The raw materials used in the experiment include hollow copper mesh (30 μm thick), sapphire substrate (80 μm thick), CNT suspension (consisting of 5% carbon nanotubes, 1% extinction powder, 10% carbon black, 13% dispersant, 5% acrylic resin and 66% water), SiC with a mesh size of 400, and single-layer $Ti_3C_2T_x$ MXene provided by Xinxi Technology Co., Ltd.

First, the CNT and MXene dispersions were mixed at the designed ratio to form a stable homogeneous dispersion; the mixture of CNTs and MXene was referred to as BP. Subsequently, the resulting mixture was loaded into the liquid storage tank of a spray gun (model: PJR116B, nozzle diameter: 0.8 mm). The spray gun was positioned at a fixed working distance of 12 cm from the substrate, with the atomization pressure regulated at 0.4 MPa throughout the spraying process. Under these conditions, the spray cone formed a circular deposition area with a diameter significantly larger than the sample size, ensuring that the sample was always positioned within the central, most stable region of the spray flux where the coating uniformity is optimal. To precisely control the coating thickness and ensure consistency between batches, the duration of each spraying cycle was strictly fixed at 10 seconds. After a single spraying, the sample was immediately transferred to a constant temperature heating stage preset at 80 ℃ and left to stand for 5 minutes to initially dry the coating and remove residual solvents.

After the BP layer solidified, SiC particles were spread on its surface and left for 5 minutes to combine with the BP layer, and then the excess uncombined SiC particles were removed. Thus, the construction of one BP-SiC double-layer unit was completed. According to the preset design, the above "spraying-drying-deposition" cycle was repeated until the target number of layers and total thickness were achieved. Fig. 1 shows the preparation process of the CNTs/MXene-SiC coating and devices.

To systematically study the effect of structure on absorption performance, a total of 8 types of material coating samples with different architectures were prepared in this study, including 3 samples deposited on Si substrates (for transmittance characterization) and 5 samples deposited on Au-coated Si substrates (for reflectivity characterization). In addition, 3 types of device samples (Detectors A, B, and C) were fabricated on MCNO thermistor substrates for optoelectronic performance evaluation. Since repeated spraying would lead to thickening of the coating, the material coating samples were prepared with more repeated cycles (up to 8 layers), while only 2 layers of the sandwich structure were applied in device preparation to maintain a low thermal time con-

stant. The specific architectures are summarized in Table 1:

2.3 Performance Characterization and Electrical Properties

The reflectivity and absorptivity in the infrared and THz bands were tested using a VERTEX 80v instrument. The samples were analyzed by Raman spectroscopy with a Thermo Fisher Scientific DXR22xi Raman imaging microscope and a laser wavelength of 532 nm for the experiment. The surface morphology of the composite films was observed with an OLS5000 laser confocal microscope, and the SEM images were obtained with a Zeiss Sigma500 field emission scanning electron microscope.

A CS1050 blackbody source from Electro Optical Industries, a VDI WR2.2SGX 170 GHz signal source, and laser sources with wavelengths of 0.635, 1.55, and 10 μm were used for the blackbody, THz, and laser measurement experiments. The frequency-dependent re-

Table 1 Coating and device parameters
表 1 涂层与器件参数

Type	Name	Coating Structure	MXene : CNTs	Repeated Circles
Transmission Samples (Si sub)	CNTs_1	Pure CNTs Coating	Pure CNTs	1
	CNTs_2	Pure CNTs Coating	Pure CNTs	4
	CNTs_3	Pure CNTs Coating	Pure CNTs	8
Absorptive Materials (Au sub)	Material A	Pure CNTs Coating	Pure CNTs	8
	Material B	BP-SiC-BP-SiC-BP	1 : 2	3
	Material C	BP-SiC-BP-SiC-BP	1 : 4	3
	Material D	BP-SiC-BP-SiC-BP	1 : 8	3
	Material E	CNTs-SiC-CNTs(Repeats)	Pure CNTs	8
Detector	Detector A	BP-SiC-BP	1 : 2	2
	Detector B	Pure CNTs Coating	Pure CNTs	8
	Detector C	MCNO Film	None	None

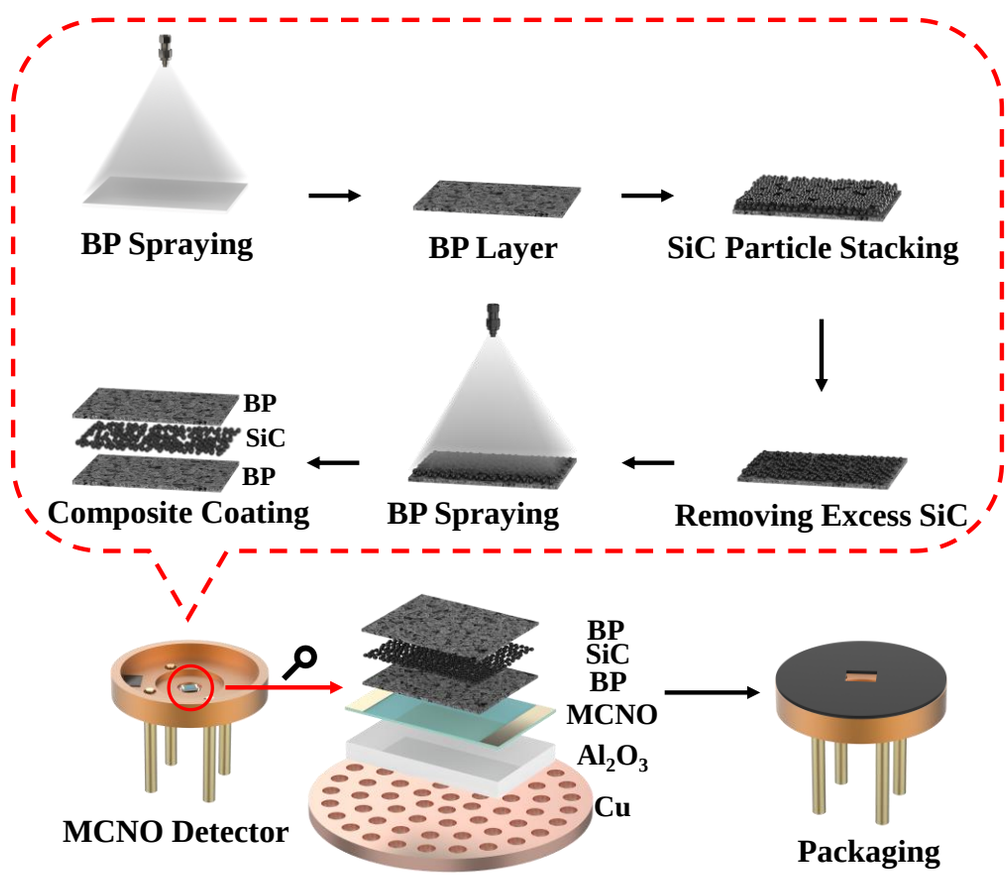

Fig. 1 Device fabrication process
图 1 器件制备工艺流程

sponse of the detector was recorded by a Stanford SR770 dynamic signal analyzer. The detector was connected to a preamplifier and powered by a ±14 V DC power supply (GPS-303C), and an alumina plate was used for shielding to measure its voltage fluctuation. In addition, the measurement of the response signal waveforms was accomplished by combining a 600 MHz TDS 3034B digital phosphor oscilloscope with a Stanford SR830 lock-in amplifier.

The IV characteristics of the MCNO sensitive element were tested. A temperature control device was used to set the test temperature at 30±0.1 ℃ with a stabilization time of ≥5 minutes to ensure uniform temperature of the sensitive element; a Keithley 2600B source meter was adopted with a voltage scanning range of ±10 V and an automatically matched current range. Since the device resistance is much higher than the lead resistance, the two-wire method was used to directly measure the device resistance, and the shell of the test device was grounded to avoid power frequency interference. The test results are shown in Fig. 2(g), and the curve shows a linear relationship between current and voltage, indicating that ohmic contact is formed between the device and the electrodes.

Subsequently, the TCR test of the material was carried out. A variable temperature probe test device and a high-precision current source meter were used to test and calibrate the room temperature resistance and the variable temperature TCR of the device. The test device consists of a high-precision electrical source meter and a variable temperature probe test station. The resistance of the MCNO sensitive element and the TCR technical index in the range of -30 – 30 ℃ were obtained through the variable temperature electrical test of standard volt-ampere characteristics. The variable temperature resistance of the MCNO device with Al_2O_3 as the substrate was obtained by the variable temperature probe station test. The final test results and the variation of TCR with temperature are shown in Fig. 2(h). The resistivity of the MCNO thin film decreases exponentially with the increase of temperature in the range of 243 – 313 K. The result shows that E is 0.29 eV, and the TCR reaches about 3.77% K^{-1} at room temperature (293 K), which is higher than the typical range of 2 – 3% reported for commercial microbolometers based on VO_x.

3 Results and Discussion

3.1 Surface Morphology and Structural Character-

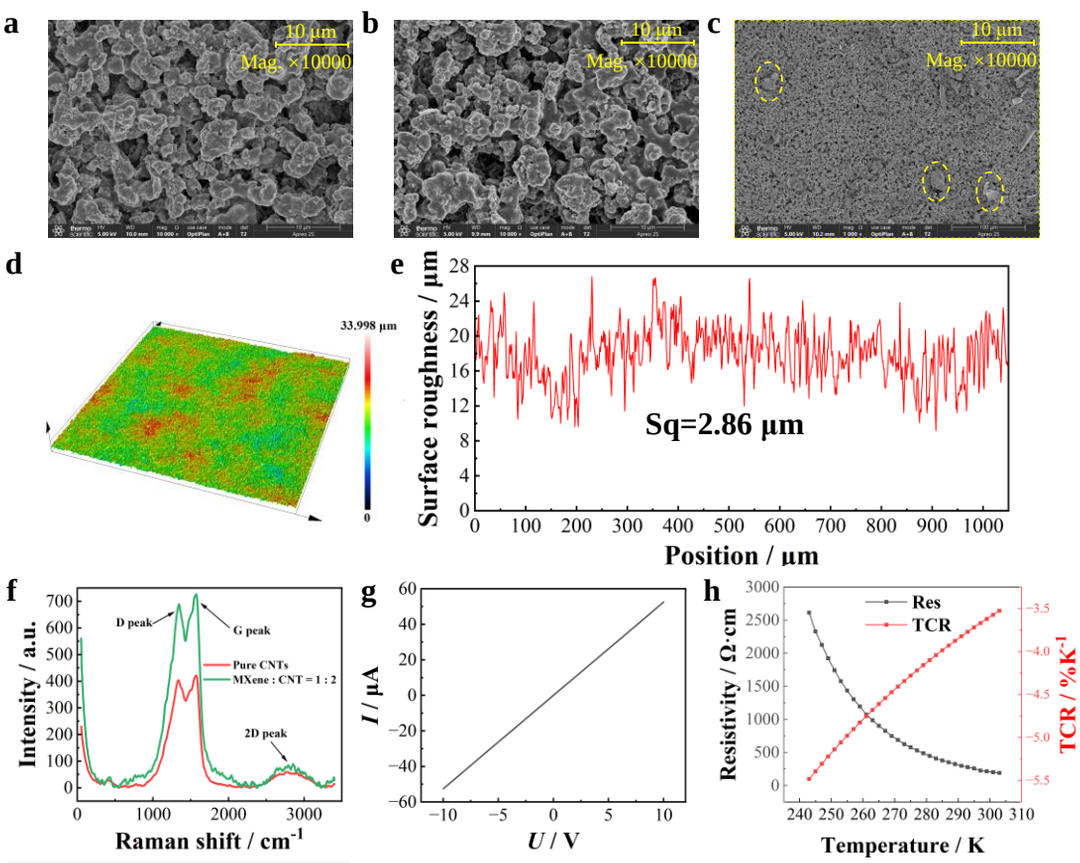

Fig. 2 Morphological, structural, electrical and thermal characterizations: (a)-(c) SEM images of Detector A, Detector B and SiC, respectively; (d) Laser confocal microscope image of Material B; (e) Roughness along a horizontal line of Material B; (f) Raman spectra of pure CNTs and MXene/CNTs composite; (g) I-V curve of MCNO; (h) Resistivity and TCR of MCNO

图 2 材料与器件的形貌、结构、电学及热学表征:(a)-(c) 分别为探测器 A、探测器 B 与 SiC 颗粒的扫描电子显微镜图像;(d) 材料 B 的激光共聚焦显微镜形貌图;(e) 材料 B 沿水平剖线的粗糙度分布;(f) 纯碳纳米管与 MXene/碳纳米管复合材料的拉曼光谱;(g) MCNO 薄膜的伏安特性曲线;(h) MCNO 的电阻率与电阻温度系数随温度的变化曲线

ization

Fig. 2(a)-(c) show the SEM images of Detector A, Detector B and SiC, respectively, and the surface morphology of Material B was characterized by laser confocal microscopy, as shown in Fig. 2(d)-(e). The root-mean-square roughness is determined to be approximately 2.86 μm, which is much smaller than both the total coating thickness and the incident THz wavelengths. The Raman spectra of CNTs and MXene/CNTs composite were compared, as shown in Fig. 2(f). In the low wave number region (0 – 1000 cm^{-1}), the signal of the composite material is significantly higher than that of pure CNTs, which is attributed to the characteristic vibration peaks of MXene such as Ti-O bonds and C-Ti bonds, directly proving that MXene has been successfully compounded with CNTs[29-31]. In the characteristic peak region of carbon nanotubes (1300 – 1600 cm^{-1}), both curves exhibit the typical D peak (~1350 cm^{-1}, corresponding to the defective and disordered structure of carbon materials) and G peak (~1580 cm^{-1}, corresponding to the in-plane vibration of sp^2 hybridized carbon)[32-34]. The intensity of the D peak and G peak of MXene/CNTs composite is significantly higher than that of pure CNTs, which may originate from two synergistic factors. First, MXene acts as a dispersant, effectively preventing CNTs agglomeration, which increases the number of scattering centres within the Raman probe volume. Second, interfacial Ti – O – C bonding may contribute via charge-transfer polarisability; meanwhile, the peak shape is dominated by the characteristics of CNTs, indicating that the introduction of MXene does not change the basic carbon skeleton structure of CNTs. In the 2D peak region (~2700 cm^{-1}), the 2D double phonon resonance peak of CNTs appears in both curves, and the intensity of the 2D peak of MXene/CNTs composites is also higher than that of pure CNTs, further confirming the structural integrity of carbon nanotubes in the composite system. Moreover, the introduction of MXene does not damage the graphitized layered structure of CNTs, but only improves the Raman response intensity through interfacial interaction. To quantitatively evaluate the interfacial interaction, the I_D/I_G intensity ratio was calculated using the peak height method after baseline subtraction. The ratio decreases from 0.96 for pristine CNTs to 0.79 for the MXene/CNTs composite. This decrease is attributed to the shielding and passivation effects of the MXene nanosheets. The MXene layers tightly wrapped around the CNT bundles, physically screening the Raman scattering from surface defects (D-band) while preserving the in-plane sp^2 vibration (G-band) of the inner CNT skeletons[35-36].

Overall, the results of SEM, laser confocal microscopy and Raman spectroscopy show that MXene and CNTs are successfully compounded with an ultra-thin thickness, and there is a significant interfacial interaction between them, providing an important basis for the subsequent analysis of the relationship between the structure and performance of the composite material.

3.2 Optical Properties

The transmittance of CNTs coatings with different layers (CNTs_1 – 3) and the reflectivity of composite coatings (Material A – E) were tested. CNTs samples with different layer counts were fabricated on Si substrates, while Material A – E were prepared on gold-coated Si substrates. The corresponding curves are shown in Fig. 3(a)-(b). The optical data were acquired by averaging 32 scans with a Fourier-transform spectrometer. For coating samples on Au substrates, the absorptivity of the coating is approximately equal to 100% minus the reflectivity. Accordingly, a lower reflectivity indicates a higher absorptivity. The transmission measurements of pure CNTs samples with different layer numbers (CNTs_1 – 3) serve as reference data to evaluate the intrinsic absorption capability of the CNTs-only absorber. The reflectivity measurements of the composite coatings (Materials A – E) serve two purposes: comparing Material A with Material E to isolate the SiC contribution (focused on 70 – 200 cm^{-1} where the difference is clearest), and comparing Materials B, C, and D with varying MXene: CNTs ratios to find the optimal composition (measured over the full 70 – 7500 cm^{-1} range). As shown in Fig. 3(b), the results demonstrate that the reflectivity in the low-frequency band decreases after adding SiC, suggesting that the introduction of the SiC interlayer enhances the wave absorption performance at low frequencies. This enhancement arises from the Mie-scattering effect of the SiC particles. Under the present particle size and wavelength conditions, the Mie scattering exhibits a dominant forward-scattering characteristic. As THz waves propagate through the coating, they undergo multiple deflections among the dispersed SiC particles, substantially extending the effective optical path within the composite medium. This prolonged transmission path significantly increases the interaction opportunities between the THz waves and both the BP matrix and the SiC particles. Consequently, electromagnetic waves that would otherwise be directly transmitted are more thoroughly absorbed, leading to a pronounced improvement in the broadband absorption efficiency of the coating. This mechanism is fundamentally distinct from simple geometric optical-path extension, as the scattering cross-section of the SiC particles in the Mie regime far exceeds their geometric cross-section. Specifically, the average absorptivity in the 70 – 130 cm^{-1} range increases by approximately 2.6% compared with the sample without SiC. The reflectivity curves of CNTs/MXene coatings with different mixing ratios are displayed in Fig. 3(c)-(d). For clarity, the reflectivity and absorptivity curves in Fig. 3(d) are offset by 5 – 20%. The results reveal that the coating with a MXene-to-CNTs mixing ratio of 1∶2 shows significantly better absorptivity than other ratios in the low-frequency band below 300 cm^{-1}.

The above results show that the introduction of the SiC intermediate layer can further optimize the absorption performance in the low frequency band; the mixing ratio of 1∶2 for MXene and CNTs can realize the optimal synergy of their layered and tubular structures, which can effectively reduce the reflection. Several MXene-based composites exhibit excellent THz absorption and

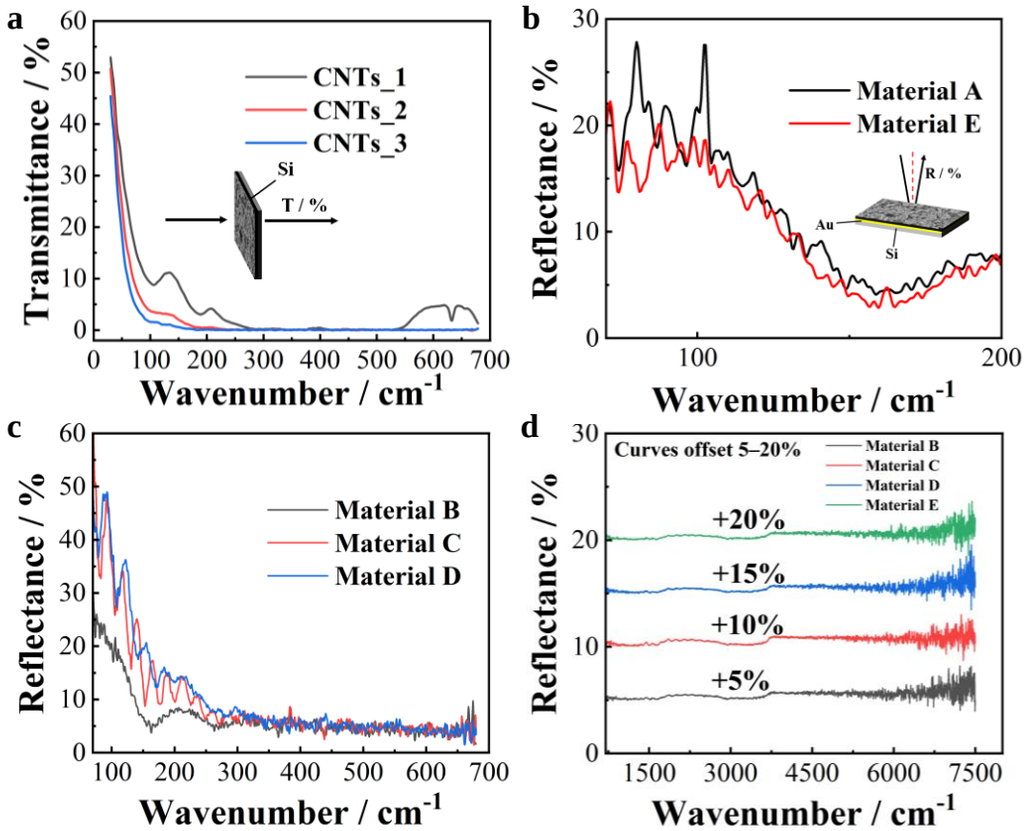

Fig. 3 Transmittance and reflectivity of the composite coatings: (a) Transmittance of CNTs_1, CNTs_2 and CNTs_3; (b) Reflectivity curves of Material A and Material E; (c) Reflectivity curves of Material B, Material C and Material D in the range of 70 – 700 cm^{-1}; (d) Reflectivity curves of Material B, Material C, Material D and Material E in the range of 700 – 7500 cm^{-1}

图 3 复合涂层的透射与反射特性:(a) CNTs_1, CNTs_2 和 CNTs_3 的透射率曲线;(b) 材料 A 与材料 E 的反射率曲线;(c) 材料 B、C、D 在 70 – 700 cm^{-1} 波段的反射率曲线;(d) 材料 B、C、D、E 在 700 – 7500 cm^{-1} 波段的反射率曲线

shielding performance, as summarized in Table 2. As shown in Fig. 3(c), distinct interference fringes can be observed in the reflection spectra of Samples B and C, which originate from interference between the front and rear surfaces of the coating. The wavenumber interval $\Delta\nu$ of the interference fringes is approximately 22 – 26 cm^{-1}. Using this value together with the coating thickness, the refractive index of the coating can be estimated to be 2.2 – 3.0. Nevertheless, uncertainties in coating thickness and errors in the interference patterns lead to considerable errors in this estimation. In the following section, the refractive index of the coating material will be extracted via the Kramers – Kronig relation using measured reflectance spectra.

To investigate the difference in absorption performance between the composite coating (Material B) and the single-component coating (Material A), and to quantitatively extract their intrinsic optical constants, we first derived the absorption coefficient α and the extinction coefficient k from the measured reflectance data using the Beer-Lambert law ($\alpha = -\frac{1}{d} lnR$, $k = \frac{\lambda\alpha}{4\pi}$, d is the coating thickness, R is the measured reflectance). Subsequently, the refractive index n was obtained via Kramers – Kronig transformation of the reflectance spectra, which is given by: $n(\omega) - 1 =$

Table 2 Terahertz absorption performance of MXene-based materials[37]

表 2 MXene太赫兹吸收性能

Material system	Thickness (mm)	Frequency (THz)	Key performance
MGOF (MXene/GO foam)	1 – 4	–	Optimal at MXene:GO=1:5
MSF (MXene/sponge foam)	2	0.3 – 1.2	>99.99% absorption at 10.5 mg
Ni/MXene-PUS	8	–	99% absorption; EMI SEA = 69.8 dB
MGF (5-layer sandwich)	0.148	0.37 – 2.0	Maximum RL = 57.7 dB
This work	0.1	2.1 – 225	Optimal at MXene:CNTs=1:2; Wideband absorption

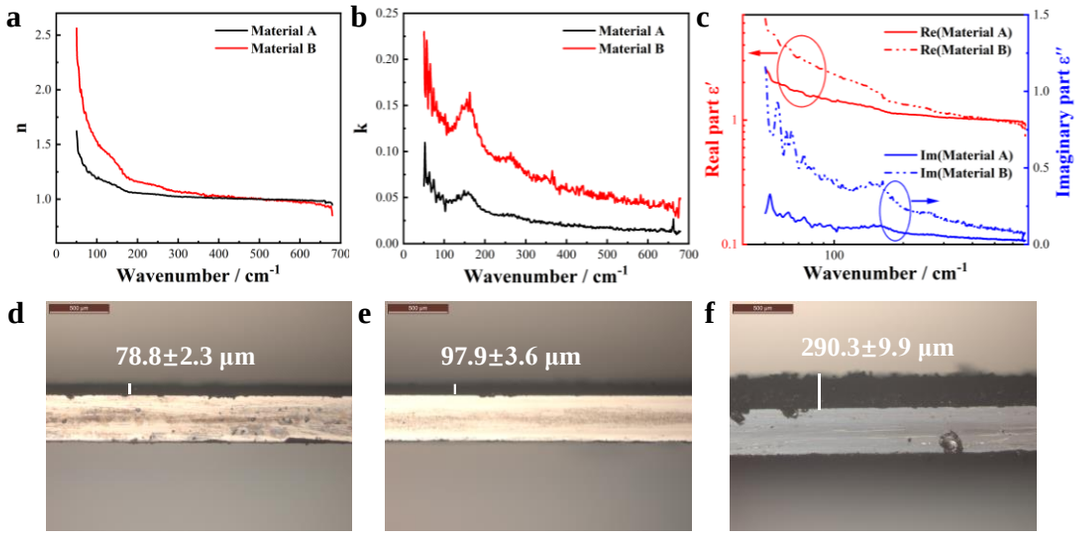

Fig. 4 Optical constants and cross-sectional morphology characterization of materials: (a)-(b) Real part n and imaginary part k of the complex refractive index extracted from the reflectance spectra of Material A and Material B via Kramers – Kronig transformation; (c) Corresponding real and imaginary parts of the complex dielectric function for Material A and Material B; (d)-(f) Cross-sectional images of 3 layers CNTs, Materials B, and Materials E, respectively, used for thickness measurement

图 4 材料的光学常数及截面形貌表征:(a)-(b) 通过 Kramers – Kronig 变换从反射光谱中提取的材料 A 和材料 B 的复折射率实部 n 与虚部 k;(c) 对应的材料 A 和材料 B 复介电函数实部与虚部;(d)-(f) 分别为 3 层 CNTs、Materials B 和 Materials E 用于厚度测量的截面图

$\frac{2}{\pi} P_c \int_0^{\infty} \frac{k(\omega')\omega' - k(\omega)}{\omega'^2 - \omega^2} d\omega$, where ω is the angular frequency and P_c denotes the Cauchy principal value, which is used to handle the singularity at $\omega' = \omega$ in the integral. On this basis, the real (ε') and imaginary (ε'') parts of the complex permittivity were calculated using $\varepsilon' = n^2 - k^2$ and $\varepsilon'' = 2nk$, respectively. As shown in Fig. 4(a)-(c), the extracted optical constants—including the real part of the refractive index n, the extinction coefficient k, and the real ε' and imaginary ε'' parts of the complex permittivity—are all distinctly higher for Material B than for Material A. Specifically, the introduction of the SiC interlayer leads to significant enhancements in both the refractive index and the dissipative components k and ε'', indicating that the composite coating not only strengthens wave – matter interactions via the increased k, but also improves impedance matching with free space through the modified n. These two effects collectively contribute to the reduced reflectivity. Notably, the simultaneous increase in ε' and ε'' suggests that the SiC particles introduce additional polarization mechanisms and scattering channels, which is highly consistent with the Mie-scattering-induced optical path extension mechanism discussed in Section 3. 4 below.

As shown in Fig. 4(e)-(f), we measured the thickness of the composite coatings at five different positions for each sample and calculated the mean values and experimental standard deviations. The results show that 3layers CNTs (3 layers, without SiC) has an average thickness of 78. 8±2. 3 μm; Material B (3 layers, with SiC interlayer) has an average thickness of 97. 9±3. 6 μm; and Material A (8 layers without SiC) has an average thickness of 290. 3±9. 9 μm. Notably, although Materials X and Y have the same number of spray-coated layers (3 layers), Material B is thicker than 3layers CNTs because Material B incorporates SiC.

3. 3 Responsivity and Detection Performance

To evaluate the THz performance of the optimal sandwich-structure device, we performed variable-carrier-frequency tests at fixed modulation frequencies. As shown in Fig. 5(a), the detector maintains stable noise performance in the frequency range of 1 – 100 Hz. The noise performance of thermal detectors is mainly determined by two parts: Johnson noise and excess noise. Here, the voltage fluctuation spectral density N_v can be expressed as: $N_v(f) = \sqrt{2k_BTR + S_v}$, where the excess noise component (S_v) is described by the Hooge empirical formula: $S_v = \frac{\gamma}{n} \cdot \frac{V_b^2}{V_d f}$. In the formula, γ is the Hooge parameter, n is the carrier concentration, V_b is the bias voltage, V_d is the detector volume, f is the frequency, and $2k_BTR$ represents the intrinsic Johnson noise. The low excess noise characteristics of the MCNO thermistor are favorable for uncooled infrared and THz detection applications.

To study the thermal sensitivity of the detector, the blackbody measurement method was adopted: a preamplifier with a chopping frequency of 1 – 12 Hz and a gain of 55000 times was used to determine the time constant of the detector. During the measurement, the detector was placed at an ambient temperature of 25 ℃, with a blackbody source having an exit hole diameter of 3 mm and an exit port distance of 12 cm. The blackbody source temperatures were set to 550, 600, 650 and 700 K, respectively, the detector bias voltage was set to 14 V, and then the amplified signal was detected.

The responsivity (R_v), and noise equivalent power (NEP) of the detector can be calculated by the following formulas: $R_v = \frac{V_s}{\phi_s} \propto \eta$[38], $NEP = N_v/R_v$ where V_s is the response voltage obtained by dividing the input value of the lock-in amplifier by the amplification gain; ϕ_s is the incident power received by the detector; N_v is the voltage fluctuation spectral density. In the blackbody measurement, the fundamental wave effective value of the incident power ϕ_s can be calculated by the following formula: $\varphi_s = \frac{\eta P_{in} A_D}{\sqrt{2}\,\pi}$, $P_{in} = \frac{\sigma(T_{bla}^4 - T_{amb}^4)A_0}{L^2}$, where P_{in} is the incident power per unit area, A_D is the effective area of the detector, η is the fundamental frequency coefficient of the square wave after Fourier transform, σ is the Stefan-Boltzmann constant, T_{bla} and T_{amb} are the blackbody temperature and ambient temperature (291 K), respectively, A_0 is the blackbody aperture area, A_D is the detector area, and L is the distance from the blackbody aperture to the detector. N_v is obtained from the noise spectrum measurement results. The response time of the detector can be obtained by fitting the data with the least square method through the following formula: $V_s \propto \frac{1}{\sqrt{1 + (2\pi f\tau)^2}}$, where τ is the thermal time constant of the detector, calculated by fitting the above formula with the least square method, and f is the radiation modulation frequency. The response current and time constant were measured as functions of blackbody temperature, from which the temperature-dependent responsivity was derived using the fitted detector resistance R_d.

The responsivity of the three samples Detector A, Detector B, Detector C is shown in Fig. 5(a), and their time constants τ are 143.7 ms, 626.7 ms, and 21.6 ms, respectively. MXene and CNTs exhibit excellent infrared absorption performance, enabling more efficient conversion of infrared radiation into thermal or electrical signals. However, for Detector B, light absorption is completed at the surface layer due to its thick CNTs coating (8 layers), and thermal conduction to the surface of the sensitive element requires a certain time. If the modulation frequency is excessively high, the thermal response cannot keep pace, resulting in a relatively large time constant. In contrast, Detector C is unmodified with any coating, leading to insufficient infrared radiation absorption capacity and thus an extremely low responsivity. Meanwhile, it can be seen that the responsivity of the 2-layer Detector A is comparable to that of the 8-layer Detector B. As shown in Fig. 5(d), the NEP of Detector A is overall very low and exhibits the least fluctuation across the entire frequency range (1 – 10 Hz), with the

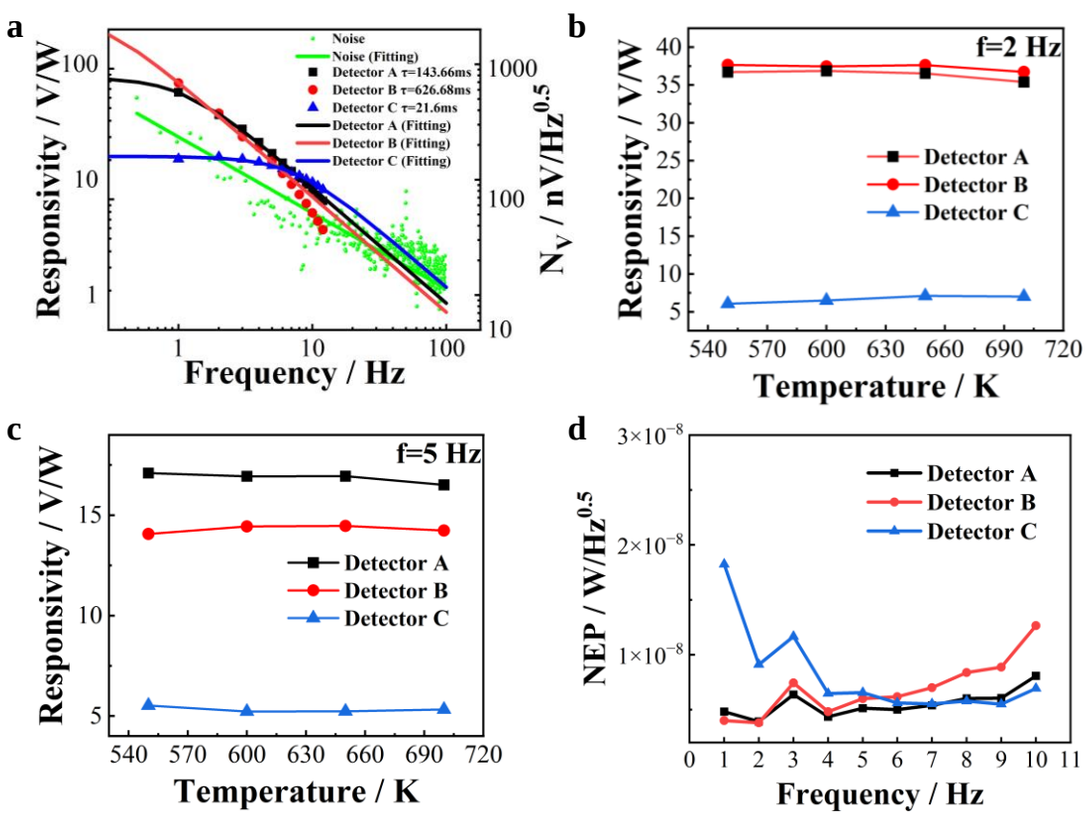

Fig. 5 Blackbody response and noise power spectral density: (a) Responsivity and noise power spectral density of the device to blackbody; (b) Responsivity at different blackbody temperatures with a modulation frequency of 2 Hz; (c) Responsivity at different blackbody temperatures with a modulation frequency of 5 Hz; (d) NEP at different modulation frequencies

图 5 器件的黑体响应与噪声特性:(a) 器件对黑体辐射的响应率与噪声功率谱密度;(b) 调制频率 2 Hz 下,不同黑体温度对应的器件响应率;(c) 调制频率 5 Hz 下,不同黑体温度对应的器件响应率;(d) 不同调制频率下的噪声等效功率

lowest value of 3×10^{-9} W/Hz$^{0.5}$ achieved at a modulation frequency of 2 Hz. The NEP of Detector B shows an overall increasing trend with rising frequency, reaching approximately 1.3×10^{-8} W/Hz$^{0.5}$ at 10 Hz. For Detector C, the NEP is relatively high at low frequencies, approaching 2×10^{-8} W/Hz$^{0.5}$ at 1 Hz.

Then the responsivity of Detector A, Detector B and Detector C at different blackbody temperatures with modulation frequencies of 2 Hz and 5 Hz was compared, with the results shown in Fig. 5(b)-(c). All responsivity values are the average of five independent measurements. The relative deviations for all data points are below 3%. The test results present a core characteristic: as the modulation frequency increases from 2 Hz to 5 Hz, the responsivity of both Detector A and Detector B decreases to varying degrees, but the decrease amplitude of Detector B′s responsivity is significantly larger than that of Detector A. This result further confirms the superiority of the "BP-SiC-BP paint" sandwich structure design. Quantitative data show that the responsivity of Detector A is about 36.5 V/W at 2 Hz and 17 V/W at 5 Hz, with a decrease amplitude of about 53%; while the responsivity of Detector B is 37.5 V/W at 2 Hz, close to that of the sandwich structure device, but drops to 14.5 V/W at 5 Hz, with a decrease amplitude of up to 61%. Notably, when normalized to unit absorber thickness, Detector A exhibits a specific responsivity of 0.61 V/(W·μm), which is approximately 3.8-fold that of Detector B (0.16 V/(W·μm)), despite their similar absolute values at 2 Hz. In contrast, the responsivity of Detector C remains extremely low throughout.

3.4 Broadband and Uniform Response of the Device

Based on the thermal detection mechanism, the responsivity R_v of a detector is positively proportional to its absorptivity (η)[38]. Broad-spectrum characteristics enable the device to achieve uniform photoresponse over a wide wavelength range. To verify this property, four independent wavelength measurements were carried out at 0.635 μm in the visible, 1.55 μm in the near-infrared, 10.6 μm in the mid-infrared, and 880 μm in the THz. For 0.635, 1.55 and 10.6 μm, the modulation frequency was varied from 1 to 25 Hz; for 880 μm, only at a fixed modulation frequency of 2 Hz. Therefore, the response uniformity among the four wavelengths was evaluated at 2 Hz. The test results are presented in Fig. 6(a)-(d).

The four independent measurements at 0.635, 1.55, 10.6 and 880μm give an average responsivity of 35.9±1.8 V/W at 2 Hz. The response uniformity is defined as $U = 1 - \sigma/\mu$, where σ is the standard deviation and μ is the mean responsivity, yielding $U \approx 95\%$. These results indicate that Detector A maintains a uniform broadband response These results indicate that Detector A maintains a uniform broadband response, as verified at 0.635, 1.55, 10.6, and 880 μm. In contrast, Detector B, which is about 4 times thicker than Detector A and shows obvious fluctuations, with responsivities of approximately 20 V/W at 0.635 μm and 25 V/W at 1.55 μm. Meanwhile, the responsivity of Detector C stays be-

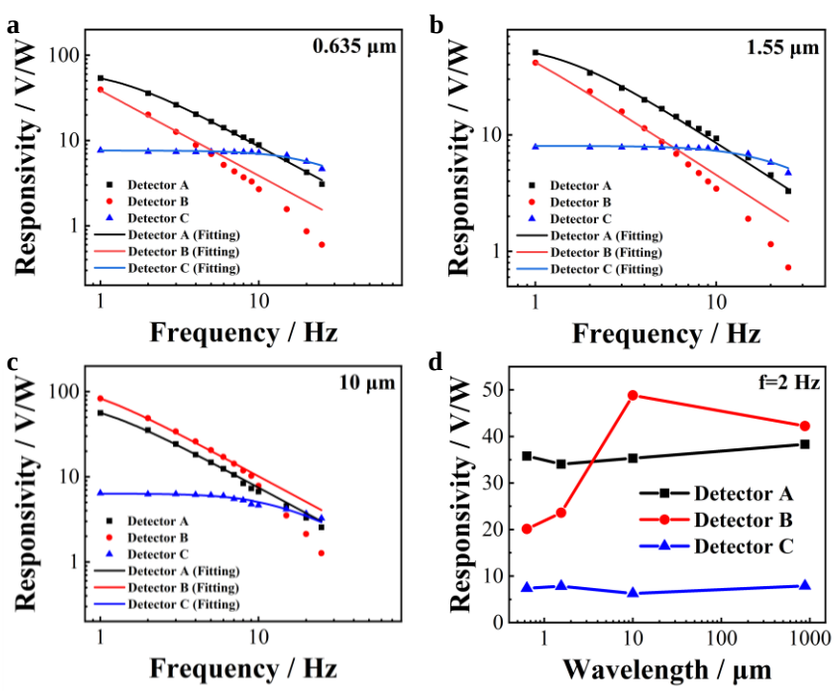

Fig. 6 Device responsivity at different wavelength bands: (a) Responsivity at a wavelength of 0.635 μm; (b) Responsivity at a wavelength of 1.55 μm; (c) Responsivity at a wavelength of 10 μm; (d) Responsivity over the wavelength range of 0.635 – 880 μm at a modulation frequency of 2 Hz

图 6 器件在不同波段的响应率:(a) 0.635 μm 波长下的器件响应率;(b) 1.55 μm 波长下的器件响应率;(c) 10 μm 波长下的器件响应率;(d) 调制频率 2 Hz 时,0.635 – 880 μm 全波段的响应率分布

low 10 V/W across all tested bands.

The performance enhancement of this sandwich-structured device originates from the synergistic optimization of the MXene/CNTs/SiC ternary composite across electrical, optical, and thermal dimensions. Electrically and optically, MXene and CNTs form a continuous conductive network, where MXene provides strong intrinsic Ohmic loss in the THz regime while CNTs contribute significant dielectric loss in the visible – near-infrared bands[44-48], collectively establishing a cascade absorption effect across the entire spectral range. The electromagnetic waves not fully absorbed by the upper layer then enter the SiC interlayer, where the high refractive index of SiC induces multiple scattering events that effectively extend the optical path, enabling the transmitted waves to be reabsorbed by the lower black paint layer—thus forming an "absorption – scattering – reabsorption" cascade pathway. Thermally, the total thickness of the composite coating is controlled at about 60 μm, ensuring high absorptivity while avoiding excessive thermal mass, which results in a relatively low thermal time constant. Owing to this triple synergistic effect, the ultrathin coating achieves stable and uniform responsivity of 0.635, 1.55, 10.6, and 880 μm.

In summary, the "BP-SiC-BP paint" sandwich structure device exhibits a response uniformity of approximately 95% at the four representative wavelengths of 0.635, 1.55, 10.6, and 880 μm. As shown in Table 3, this detector features a wider operating spectral range compared with other detectors, providing technical support for its application in multi-band integrated detection systems.

4 Conclusion

We have successfully developed a broadband MCNO bolometer based on MXene/CNTs/SiC composites with a BP-SiC-BP sandwich absorption architecture, and verified its uniform broadband response by measurements at four independent representative wavelengths from visible to THz. Its broadband absorption and detection capability originate from the synergistic cascade absorption effect of MXene/CNTs and the optical path extension induced by the SiC intermediate layer, enabling energy dissipation across a broad spectral wavelength range. Comprehensive characterizations demonstrate that the optimal ratio of MXene to CNTs in the composite BP is 1:2, and an ultrathin composite coating has been integrated on the MCNO thermosensitive substrate. The as-fabricated bolometer exhibits favorable optoelectronic properties: the absorption layer achieves low reflectivity and transmittance in the band of 150 – 7500 cm^{-1}; four independent measurements at 0.635, 1.55, 10.6 and 880 μm under 2 Hz modulation exhibit an average responsivity of 35.9± 1.8 V/W corresponding to a response uniformity of approximately 95%; and operates stably within the modulation frequency range of 1 – 25 Hz. Meanwhile, the device features an NEP of 3×10^{-9} $W/Hz^{0.5}$ and a suitable thermal time constant of approximately 143.7 ms, showing advantages over pure CNTs-modified and unmodified MCNO detectors. This work provides a novel design strategy and feasible technical route for the development of broadband thermal detectors, and offers key support for the application of broadband detection technology in non-destructive imaging, biosensing, next-generation communication and other fields. Future research can further optimize the coating preparation process to improve the integration and detection performance of the device.

Table 3 Comparison between this work detector and other detectors
表3 本工作探测器与其他探测器对比

Device type	Spectral band(μm)	NEP($WHz^{-1/2}$)	Response time(s)	Cooling Condition	Ref.
NPG-VO_2	3 – 12 (MIR)	~10^{-13}	~0.001	Uncooled	[39]
MCT e-APD	1 – 4 (NIR – MIR)	~10^{-15}	~10^{-6}	Cooled	[40]
InGaAs	0.6 – 1.7 (VIR-NIR)	~10^{-13}	~10^{-10}	Cooled/Uncooled	[41]
InSb	1 – 5.5 (NIR – MIR)	~10^{-13}	~10^{-7}	Cooled	[41]
Si:Ga BIB	14 – 20 (MIR)	~10^{-13}	~10^{-4}	Cooled	[42]
Golay cell	25 – 750 (FIR/THz)	~10^{-9}	~0.01	Uncooled	[43]
This work	0.635, 1.55, 10.6 and 880(VIR – FIR/THz)	~10^{-9}	~0.1	Uncooled	–

References

[1] Israelowitz M, Weyand B, Schmitz G, et al. Biomimetic optics in the infrared and terahertz wavelengths for clinical applications [J]. Journal of Bionic Engineering. 2025; 22(5): 2338-2353. http://doi.org/10.1007/s42235-025-00749-x.

[2] Si W, Zhou W, Liu X, et al. Recent advances in broadband photodetectors from infrared to terahertz [J]. Micromachines. 2024;15(4):427. http://doi.org/10.3390/mi15040427.

[3] Chen T, Han Z, Liu J, et al. Terahertz gas sensing based on a simple one-dimensional photonic crystal cavity with high-quality factors [J]. Applied Optics. 2014;53(16): 3454-3458. http://doi.org/10.1364/ao.53.003454.

[4] Sizov FF, Reva VP, Golenkov AG, et al. Uncooled detectors challenges for THz/sub-THz arrays imaging [J]. Journal of Infrared, Millimeter, and Terahertz Waves. 2011; 32(10): 1192-1206. http://doi.org/10.1007/s10762-011-9789-2.

[5] Davies AG, Burnett AD, Fan W, et al. Terahertz spectroscopy of explosives and drugs [J]. Materials Today. 2008; 11(3): 18-26. http://doi.org/10.1016/s1369-7021(08)70016-6.

[6] M, Singh G. Terahertz imaging and sensing for healthcare: current status and future perspectives [J]. IEEE Access. 2023; 11: 1-30. http://doi.org/10.1109/ACCESS.2023.3247196.

[7] Wang X R, Fan X H, Liu Y C, et al. 3D nanolithography via holographic multi-focus metalens [J]. Laser & Photonics Reviews, 2024, 18(11): 2400181. https://doi. org/10.1002/lpor.202400181.

[8] Tan Y S, Wang H, Wang H T, et al. High-throughput fabrication of large-scale metasurfaces using electron-beam lithography with SU-8 gratings for multilevel security printing [J]. Photonics Research, 2023, 11(3): B103-B110. https://doi. org/10.1364/PRJ.472212.

[9] Zheng RN, Hou HG, Lv QJ, Jiang JL, Gong JH, Liu GW, Liu JL, Qiao GJ. Construction and photothermal properties of microsphere-modified cavity resonator absorbers with ultra-wide infrared spectrum absorption [J]. Infrared Physics & Technology. 2026; 154: 106425. https://doi. org/10.1016/j. infrared. 2026.106425.

[10] Xie Y, Lv QJ, Chen TZ, Zhang DL, Liu SW, Hou HG, Liu GW, Qiao GJ, Liu JL. TiN nanoparticles anchored on porous carbon black: the synergistic effect of porosity, surface roughness and surface plasmon on high-performance broadband infrared absorption [J]. Infrared Physics and Technology. 2025; 138: 105819. https://doi.org/10.1016/j.infrared.2025.105819.

[11] Huo T, Yin H, Zhou D, et al. Self-powered broadband photodetector based on single-walled carbon nanotube/GaAs heterojunctions [J]. ACS Sustainable Chemistry & Engineering. 2020; 8(41): 15532-15539. http://doi. org/10.1021/acssuschemeng.0c04495.

[12] Wang K, Wang F, Cao Y, et al. High-performance photodetectors based on suspended ultralong CNTs-MoS_2 heterojunction networks [J]. Advanced Functional Materials. 2024; 35(15): 2421980. http://doi.org/10.1002/adfm.202421980.

[13] Yin J, Singh R, Chen M, et al. Carbon nanotube-based electrically tunable broadband terahertz absorbers [J]. Optical Materials. 2023;139. http://doi.org/10.1016/j.optmat.2023.113779.

[14] Wang R, Xie L, Hameed S, et al. Mechanisms and applications of carbon nanotubes in terahertz devices: a review [J]. Carbon. 2018;132:42-58. http://doi.org/10.1016/j.carbon.2018.02.005.

[15] Sun L, Zhu M, Zhao C, et al. Wafer-scale vertically aligned carbon nanotubes for broadband terahertz wave absorption [J]. Carbon. 2019; 154: 503-509. http://doi. org/10.1016/j. carbon.2019.08.001.

[16] Amemiya K, Shimizu Y, Koshikawa H, et al. Supreme-black levels enabled by touchproof microcavity surface texture on anti-backscatter matrix [J]. Science Advances. 9(2): eade4853. http://doi.org/10.1126/sciadv.ade4853.

[17] Khazaei M, Arai M, Sasaki T, et al. Novel electronic and magnetic properties of two-dimensional transition metal carbides and nitrides [J]. Advanced Functional Materials. 2012; 23(17): 2185-2192. http://doi.org/10.1002/adfm.201202502.

[18] Song W, Liu Q, Chen J, et al. Interface engineering Ti_3C_2 MXene/silicon self-powered photodetectors with high responsivity and detectivity for weak light applications [J]. Small. 2021; 17(23): 2100439. http://doi.org/10.1002/smll.202100439.

[19] Zhao T, Xie P, Wan H, et al. Ultrathin MXene assemblies approach the intrinsic absorption limit in the 0.5 – 10 THz band [J]. Nature Photonics. 2023;17(7):622-628. http://doi.org/10.1038/s41566-023-01197-x.

[20] Li X, Luo H. Maximizing terahertz energy absorption with MXene absorber [J]. Nano-Micro Letters. 2023;15(1):198. http://doi.org/10.1007/s40820-023-01167-6.

[21] Zhang X, Shao J, Yan C, et al. High performance broadband self-driven photodetector based on MXene ($Ti_3C_2T_x$)/GaAs Schottky junction [J]. Materials & Design. 2021; 207. http://doi. org/10.1016/j.matdes.2021.109850.

[22] Yue Y, Wang Y, Xu X, et al. Graphite-ring-stacked carbon nanotubes synthesized during the rescue of $Ti_3C_2T_x$ MXene for dual-peak electromagnetic wave absorption [J]. Journal of Alloys and Compounds. 2023; 945. http://doi. org/10.1016/j. jallcom. 2023.169342.

[23] Zhang X, Zhang ZW. Fabrication and performance of a $NiMn_2O_4$/$LaNiO_3$ composite film detector with multi electrodes for night vision imaging application [J]. Sensors and Actuators A: Physical. 2021; 326: 112713. http://doi. org/https://doi. org/10.1016/j.sna.2021.112713.

[24] Yin Y, Wu J, Zhou W, et al. Post annealing effects on low temperature deposited Mn-Co-Ni-O films by radio frequency magnetron sputtering [J]. Materials Letters. 2019; 235: 172-175. http://doi.org/https://doi.org/10.1016/j.matlet.2018.10.046.

[25] Wu C, Zhou W, Yin Y, et al. Long wavelength infrared detection based on Mn-Co-Ni-O thin films with dielectric-metal-dielectric absorptive structures [J]. Infrared Physics & Technology. 2019; 102: 102987. http://doi.org/https://doi.org/10.1016/j.infrared.2019.102987.

[26] He L, Ling ZY, Wu MY, et al. Thermal and humidity sensing behaviors of $Mn_{1.85}Co_{0.3}Ni_{0.85}O_4$ thin films: effects of adjusting the surface morphology [J]. Applied Surface Science. 2017; 410: 201-205. http://doi.org/https://doi.org/10.1016/j.apsusc.2017.03.101.

[27] Chen L, Zhang Q, Yao J, et al. Formation of Mn-Co-Ni-O nanoceramic microspheres using in situ ink-jet printing: sintering process effect on the microstructure and electrical properties [J]. Small. 2016;12(36):5027-5033. http://doi.org/https://doi.org/10.1002/smll.201600470.

[28] Kumar A, Dubey SK, Kumar A, et al. A near infrared MIM metamaterial absorber using SiC [J]. Photonics and Nanostructures - Fundamentals and Applications. 2024; 58: 101226. http://doi.org/https://doi.org/10.1016/j.photonics.2024.101226.

[29] Zhang L, Su W, Huang Y, et al. In situ high-pressure X-ray diffraction and Raman spectroscopy study of $Ti_3C_2T_x$ MXene [J]. Nanoscale Research Letters. 2018; 13(1): 343. http://doi.org/10.1186/s11671-018-2746-4.

[30] Liu Z-W, Wang G, Li Y-F, et al. Substrate types and applications of MXene for surface-enhanced Raman spectroscopy [J]. Frontiers in Chemistry. 2024; 12. http://doi. org/10.3389/fchem.2024.1378985.

[31] Minassian H, Melikyan A, Goncalves MR, et al. $Ti_3C_2T_x$ MXene as a surface-enhanced Raman scattering substrate [J]. Beilstein

Archives. 2023:202338. http://doi.org/10.3762/bxiv.2023.38.v1.
[32] Jorio A, Pimenta MA, Filho AGS, et al. Characterizing carbon nanotube samples with resonance Raman scattering [J]. New Journal of Physics. 2003; 5: 139. http://doi.org/10.1088/1367-2630/5/1/139.
[33] Dresselhaus MS, Dresselhaus G, Saito R, et al. Raman spectroscopy of carbon nanotubes [J]. Physics Reports. 2005; 409(2): 47-99. http://doi.org/10.1016/j.physrep.2004.10.006.
[34] Jorio A, Ferrari A, Robertson J, Saito R, et al. Determination of nanotubes properties by Raman spectroscopy [J]. Philosophical Transactions of the Royal Society of London Series A: Mathematical, Physical and Engineering Sciences. 2004; 362(1824): 2311-2336. http://doi.org/10.1098/rsta.2004.1443.
[35] Ding M, Liu H, Jiang H, et al. Raman spectrum of MXene Ti_2C under planar symmetrical strain: first-principles calculations [J]. Journal of Raman Spectroscopy. 2022; 53 (11): 1915-1923. http://doi.org/10.1002/jrs.6432.
[36] Songsart-Power M, Wilson B, Phalen JW, Dhital C, et al. Surface-enhanced Raman scattering on two-dimensional Nb_2CT_x MXene [J]. Applied Physics Letters. 2025; 126 (20): 201101. http://doi.org/10.1063/5.0262640.
[37] Wu Y F, Zhang X L, Li H, et al. MXene materials for terahertz applications: a review [J]. Optoelectronics Letters, 2024, 20(5): 272-288. https://doi.org/10.1007/s11801-024-3091-8.
[38] Richards PL. Bolometers for infrared and millimeter waves [J]. Journal of Applied Physics. 1994; 76(1): 1-24. https://doi.org/10.1063/1.357128.
[39] Shabbir MW, Chandra S, Leuenberger MN. Numerical simulations of nanolayered heterostructures of nanopatterned graphene and vanadium oxide for mid-infrared photodetectors operating close to room temperature [J]. ACS Applied Nano Materials, 2022, 5(2): 2189-2197. https://doi.org/10.1021/acsanm.1c03809.
[40] Refaat TF, Petros M, Remus R, et al. MCT APD detection system for atmospheric profiling applications using two-micron lidar [C]. EPJ Web of Conferences, 2020, 237: 01013. https://doi.org/10.1051/epjconf/202023701013.
[41] Rogalski A. Infrared detectors: status and trends [J]. Progress in Quantum Electronics. 2003; 27(2-3): 59-210. http://doi.org/10.1016/s0079-6727(02)00024-1.
[42] Deng K, Guo D, Zhang K, et al. Synergistic Light Localization Enhanced CMOS - Compatible Detectors With Infrared Detection Wavelength up to 20 μm [J]. Advanced Functional Materials. 2026; 36(72): 1. http://doi.org/10.1002/adfm.202532129.
[43] Philippov MV. Scientific equipment for the space experiment "Sun-Terahertz": methods for increasing the frequency selectivity of detectors [J]. Measurement Techniques. 2025; 68(3/4): 209-219. https://doi.org/10.1007/s11018-025-02442-1.
[44] Satapathy A, Sawant KK, Mondal S, et al. Recent progress on MXenes as an attenuator of terahertz radiation [J]. Journal of Electronic Materials. 2022; 52(3): 1749-1768. http://doi.org/10.1007/s11664-022-10098-8.
[45] Zhao T, Wan H, Zhang T, et al. Mechanism of the terahertz wave – MXene interaction and surface/interface chemistry of MXene for terahertz absorption and shielding [J]. Accounts of Chemical Research. 2024; 57(15): 2184-2193. http://doi.org/10.1021/acs.accounts.4c00326.
[46] Fei Y, Wang Q, Wang F, et al. M-site dependent terahertz intrinsic absorption in MXenes [J]. InfoMat. 2025; 7(4): e12654. http://doi.org/10.1002/inf2.12654.
[47] Zhu L, Wu W, Chen J, et al. High-performance electromagnetic wave absorption by two-dimensional mesoporous monolayer $Ti_3C_2T_x$ MXene [J]. Chemical Engineering Journal. 2024; 488. http://doi.org/10.1016/j.cej.2024.150649.
[48] Li S, Xu S, Pan K, et al. Ultra-thin broadband terahertz absorption and electromagnetic shielding properties of MXene/rGO composite film [J]. Carbon. 2022; 194: 127-139. http://doi.org/https://doi.org/10.1016/j.carbon.2022.03.048.

基于 MXene/CNTs/SiC 复合材料的可见–太赫兹宽带均匀响应 MCNO 测辐射热计

陈 兵[1,2]，高艳卿[2,3]，雷思源[2,3]，池灵泽[1,2]，冷成宇[6]，杨 波[5]，江 林[3]，姚娘娟[3]，刘 奕[2,4]，周 炜[2,3*]，印雄飞[1,2*]，黄志明[1,2,3*]，褚君浩[3]

（1. 国科大杭州高等研究院，杭州 310024；
2. 中国科学院大学，北京 100049；
3. 中国科学院上海技术物理研究所 红外物理国家重点实验室，上海 200083；
4. 中国科学院宁波材料技术与工程研究所，宁波 315201；
5. 华中科技大学物理学院，武汉 430074；
6. 上海大学微电子学院，上海 201804）

摘要：宽带探测器的发展对无损成像、生物传感及下一代通信等应用至关重要。本文研制了一种基于 MXene/CNTs/SiC 复合吸收层的宽带 $Mn_{1.56}Co_{0.96}Ni_{0.48}O_4$（MCNO）测辐射热计，并在四个代表性波长处验证了其均匀响应特性。设计了一种超薄"黑漆-碳化硅-黑漆"三明治结构复合吸收涂层，其中黑漆由 MXene 与碳纳米管按 1:2 的比例混合制备。具有该吸收层的 MCNO 探测器在 2 Hz 调制频率下，对 0.635、1.55、10.6 和 880 μm 四个波段独立测量下得到的平均响应率为 35.9±1.8 V/W，响应均匀性约 95%。其宽带响应源于 MXene/CNTs 复合材料的级联吸收效应以及 SiC 中间层诱导的光程延长。相应地，该器件的噪声等效功率约为 3×10^{-9} W/Hz$^{0.5}$，热时间常数约为 143.7 ms。

关 键 词：宽带光电探测器；MCNO 测辐射热计；MXene/CNTs/SiC 复合材料；可见－太赫兹波段

中图分类号：TN215 **文献标识码**：A